Space-Time-Modulated Metasurfaces with Spatial Discretization: Free-Space N-Path Systems

Zhanni Wu, Cody Scarborough, and Anthony Grbic*

Department of Electrical Engineering and Computer Science, University of Michigan, Ann Arbor, Michigan 48109-2122, USA

(Received 4 June 2020; revised 6 November 2020; accepted 10 November 2020; published 21 December 2020)

This work theoretically and experimentally studies metasurfaces with spatially discrete, traveling-wave modulation (SDTWM). A representative metasurface is considered consisting of columns of time-modulated subwavelength unit cells, referred to as stixels. SDTWM is achieved by enforcing a time delay between temporal waveforms applied to adjacent columns. In contrast to the continuous traveling-wave modulation commonly assumed in studies of space-time metasurfaces, here the modulation is spatially discretized. In order to account for the discretized spatial modulation, a modified Floquet analysis is introduced based on a new boundary condition that has been derived for SDTWM structures. The modified Floquet analysis separates the scattered field into its macroscopic and microscopic variations. The reported theoretical and experimental results reveal that the electromagnetic behavior of a SDTWM metasurface can be categorized into three regimes. For electrically large spatial-modulation periods, the microscopic field variation across each stixel can be neglected. In this regime, the space-time metasurface allows simultaneous frequency translation and angular deflection. When the spatial-modulation period on the metasurface is electrically small, the microscopic variation results in unique metasurface capabilities such as subharmonic mixing. When the spatial-modulation period of the metasurface is wavelength scale, the metasurface allows both subharmonic mixing and angular deflection to be achieved simultaneously. To verify our analysis, a dual-polarized, spatiotemporally modulated metasurface, is developed and measured at X-band frequencies.

DOI: 10.1103/PhysRevApplied.14.064060

I. INTRODUCTION

Metasurfaces are two-dimensional (2D) structures textured at a subwavelength scale to achieve tailored control of electromagnetic waves. Developments in tunable electronic components have allowed dynamic control over the electromagnetic properties of metasurfaces. Electronic devices such as varactors, transistors, and MEMS [1–5], as well as 2D and phase-change materials [6–9] can be integrated into metasurfaces to tune their electric, magnetic, and magnetoelectric responses. Often, the properties of a metasurface are spatially modulated to shape electromagnetic wavefronts and achieve focusing, beam steering, and polarization control [10–13]. By incorporating tunable elements into their design, the properties of metasurfaces can also be modulated in time [14–16]. While spatial modulation redistributes the plane-wave spectrum of the scattered field, temporal modulation provides control over the frequency spectrum. Simultaneous spatial and temporal variation is known as spatiotemporal modulation, and has recently been applied to metasurfaces [17–26]. Space-time modulation can simultaneously allow frequency conversion and beam steering and shaping. It can also be used to break Lorentz reciprocity and enable magnetless nonreciprocal devices including gyrators, circulators, and isolators [27–31].

Most papers to date have examined space-time metasurfaces with a traveling-wave modulation that is a continuous function of space. The unit-cell size of metasurfaces is assumed to be deeply subwavelength and the effect of the unit-cell size on the space-time modulated system is neglected. Here, metasurfaces with spatially discrete, space-time modulation are considered. In particular, spatially discrete traveling-wave modulation (SDTWM) of metsurfaces is explained. SDTWM structures have a spatial-modulation period made up of a finite number (N) of unit cells. The unit cells within each spatial modulation period is referred to as stixels [32]: space-time pixels of the structure. They are the smallest indivisible element of SDTWM structures. In SDTWM, the modulation of adjacent stixels is staggered by a time delay of T_p/N, where T_p is the temporal modulation period of each stixel.

The SDTWM scheme is reminiscent of that used in N-path circuit networks [33–38]. These circuit networks have gained strong interest in recent years within the circuits

*agrbic@umich.edu

community for their ability to realize high-fidelity filters [36,39,40] and nonreciprocal devices [30,35,41,42]. Leveraging this close relation, and exploiting our earlier work on N-path circuits [33] and the interpath relation [43,44], a modified Floquet-boundary condition governing fields on SDTWM metasurfaces is reported here. The modified Floquet-boundary condition accounts for the frequency-dependent Bloch wave number induced across a stixel.

The electromagnetic fields on linear electromagnetic structures that vary periodically in space and time can be modeled with a double Floquet expansion in both time and space. This generalized method of analysis can be used to solve the field distribution on any linear, periodic space-time modulated structure. It has been used recently to compute the fields scattered from space-time gratings [23]. For SDTWM structures, the interpath relation can be used to compress the double Floquet expansion, leading to a number of simplifications. Applying the interpath relation to the double Floquet expansion of fields reveals that a number of the field amplitudes become zero. Specifically, it is shown that the interpath relation reduces the number of unknown Floquet harmonics by the number of paths (N): stixels within a spatial-modulation period. Therefore, the interpath relation dramatically reduces the numerical complexity of analyzing these structures. Applying the interpath relation to the double Floquet expansion also allows the fields scattered by the SDTWM structure to be separated into its macroscopic and microscopic spatial variations. The macroscopic variation describes the field variation between respective points in stixels separated by a spatial modulation wavelength. This macroscopic variation is consistent with the field variation of continuously modulated structures and is characterized by the modulation frequency ω_p and modulation wave number $\beta_p = 2\pi/\lambda_p$. The microscopic field variation accounts for the field variation across a stixel. The microscopic variation is characterized by spatial harmonics of the modulation wave number $\beta_d = 2N\pi/\lambda_p = 2\pi/d_0$, where d_0 is the stixel (unit-cell) size.

Separating the scattered field into its macroscopic and microscopic variation, through the interpath relation, also reveals the underlying physics of SDTWM structures. The field relations reveal three regions of operation for SDTWM metasurfaces, those with small, large, and wavelength-scale spatial-modulation periods. When the spatial-modulation period is small with respect to the wavelength of radiation, low-order temporal harmonics (frequencies) are evanescent and adhere to the metasurface, while higher-order temporal harmonics specularly scatter due to aliasing. This can lead to specular subharmonic mixing. Such a phenomenon cannot be predicted by continuous space-time analysis of metasurfaces. SDTWM metasurfaces with large spatial-modulation periods behave much like spatially continuous traveling-wave-modulated

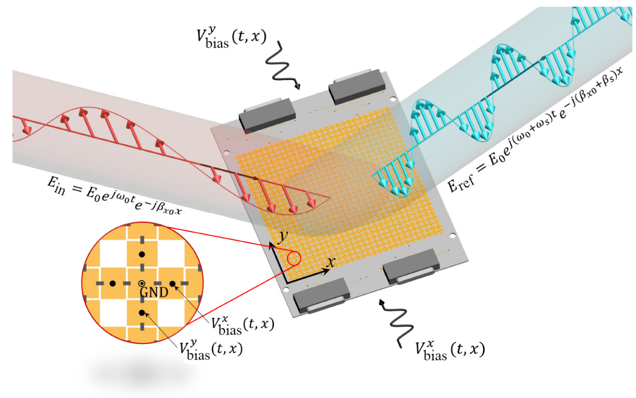

FIG. 1. A proof-of-principle SDTWM metasurface. Based on the spatial-modulation period, three regimes of operations are supported by the metasurface.

structures. Scattered waves can be deflected to different angles, and nonreciprocal responses observed. Finally, wavelength-scale spatial periods allow both deflection (scattering to nonspecular directions) and subharmonic frequency mixing. In other words, large and small spatial-period effects can be observed simultaneously. By clearly defining each regime and the effect of unit-cell size, this research can provide guidance on practically designing traveling-wave-modulated metasurfaces with spatially discrete unit cells.

To aid in the discussion of SDTWM metasurfaces, a representative example is considered throughout the paper. The reflective metasurface is shown in Fig. 1, and is based on the high-impedance surface [45]. Varactor diodes are surface mounted onto the metasurface, acting as tunable capacitances. This metasurface was presented in Ref. [16] where the varactor diodes on each column were temporally modulated with the same bias signal. In Ref. [16], a sawtooth reflection phase in time was applied to the metasurface, resulting in Doppler-like (serrodyne) frequency translation. Structures of a similar design have been subsequently reported in Ref. [46]. The metasurface consists of discrete unit cells. Each column of unit cells on the metasurface can be independently temporally modulated, allowing space-time modulation of its reflection phase. Here, only spatially discrete, traveling-wave modulations of the metasurface are considered. The metasurface is homogenized within each stixel to allow for semianalytical scattering analysis. Measurements of an experimental metasurface prototype are presented in order to verify the theory (spectral-domain analysis) used to predict the electromagnetic response of SDTWM metasurfaces.

II. ANALYSIS OF A FREE-SPACE N-PATH-MODULATED METASURFACE

A representative metasurface is introduced in this section. The SDTWM metasurface consists of a tunable

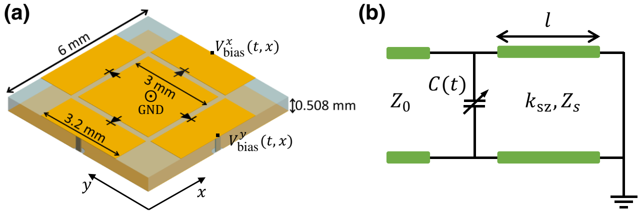

FIG. 2. (a) A stixel (unit cell) of the dual-polarized, spatiotemporally modulated metasurface. (b) The equivalent circuit model for each polarization.

capacitive sheet above a grounded dielectric substrate, as shown in Fig. 1. It is a reflective, electrically tunable impedance surface [45], which allows independent control of the reflection phase for two orthogonal polarizations. The capacitive sheet is realized as an array of metallic patches interconnected by varactor diodes. It can be modulated in both space (discretely) and time with a bias signal that is applied through the metallic vias that penetrate the substrate.

The stixel (unit cell) of the designed metasurface is shown in Fig. 2(a). The varactor diodes connecting the metallic patches are biased through the vias located at the edges of the unit cells, while the via at the central patch is connected to ground. The remainder of the biasing network is shielded behind the ground plane. The biasing network and diode orientations allow the reflection phase of the metasurface to be independently tuned for two orthogonal (TE and TM) polarizations. Bias waveforms $V^x_{\text{bias}}(t,x)$ and $V^y_{\text{bias}}(t,x)$, shown in Fig. 1, control the sheet capacitance for the two orthogonal polarizations. A detailed description of the fabrication and biasing network are provided in Sec. IV. A cross section of the metasurface is shown in Fig. 3 under TE and TM excitations. The biasing vias can be seen perforating the dielectric substrate.

In this section, we derive a semianalytical procedure for computing the response of the SDTWM metasurface shown in Fig. 1. This includes the homogenization of the representative metasurface; an introduction to the interpath relation that relates the fields of each stixel within a spatial period of SDTWM metasurface; and the resulting modified Floquet expansion of the field for a SDTWM structure.

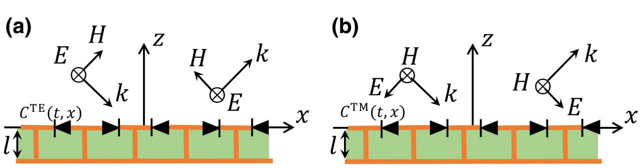

FIG. 3. Cross sections of the obliquely illuminated time-modulated metasurface, under (a) TE polarization, and (b) TM polarization.

A. Homogenization of the proposed SDTWM metasurface

In the analysis that follows, the stixels of the metasurface are homogenized to simplify the analysis and allow conclusions to be made about the general behavior of SDTWM systems. Within each stixel, the metallic patches interconnected by varactor diodes are treated as a capacitive sheet. This sheet can be modulated in time, independently of adjacent stixels. The dielectric substrate, that is perforated by vias ($-l < z < 0$), is treated as a uniaxial anisotropic material, with a relative permittivity tensor [47]:

$$\overline{\overline{\epsilon_r}} = \begin{pmatrix} \epsilon_h & 0 & 0 \\ 0 & \epsilon_h & 0 \\ 0 & 0 & \epsilon_{zz} \end{pmatrix}, \tag{1}$$

where ϵ_h is the relative permittivity of the host medium and ϵ_{zz} is the effective relative permittivity along the vias. Since the metasurface is electrically thin at the operating frequency of 10 GHz ($l = 0.016\lambda = 0.508$ mm), a local model can be used to describe the perforated substrate [47]:

$$\epsilon_{zz} = \epsilon_h \left(1 - \frac{k_p^2}{k_0^2 \epsilon_h}\right), \tag{2}$$

where $k_p = 541.81$ rad m^{-1} is the plasma wave number of the wire medium extracted from a full-wave simulation of the unit cell shown in Fig. 2(a), and k_0 is the free-space wave number of the incident wave. The anisotropic substrate supports TE (ordinary mode) and TM (extraordinary mode) polarizations. The normal wave number for each polarization in the substrate can be written as

$$k_{sz}^{\text{TE}} = \sqrt{k_0^2 \epsilon_h - k_x^2}, \tag{3}$$

$$k_{sz}^{\text{TM}} = \sqrt{k_0^2 \epsilon_h - k_x^2 \frac{\epsilon_h}{\epsilon_{zz}}}, \tag{4}$$

where k_x is the tangential wave number of the incident wave.

Each stixel can be modeled with the shunt resonator circuit depicted in Fig. 2(b). The circuit model consists of a tunable capacitance (representing the capacitive sheet) backed by a shorted transmission-line section (representing the conductor-backed dielectric substrate) that acts as an inductance. As a result, the bias voltage applied to the varactor diodes can be used to tune the reflection phase. The phase range of this topology is $2\pi - \Delta\phi$, where $\Delta\phi$ is the round-trip phase delay through the substrate. Details on the phase range of the realized metasurface are provided in Sec. IV. In this paper, two different reflection-phase waveforms are considered. A sawtooth reflection phase with respect to time is studied, which allows serrodyne frequency translation [15,16], as well as a sinusoidal reflection phase with respect to time.

As mentioned earlier, each column of unit cells can be biased independently, allowing for space-time modulation along a single (x) axis. As a result, the homogenized model consists of capacitive strips whose widths are given by the stixel size $d_0 = \lambda_0/5 = 6$ mm, where λ_0 is the wavelength in free space at 10 GHz. The capacitance seen by each polarization can be controlled independently and is uniform over the strip.

B. Interpath relation for SDTWM metasurfaces

The SDTWM modulation can be applied to the metasurface by introducing a time delay between the capacitance modulation applied to adjacent columns. This modulation scheme is shown in Fig. 4. There are N columns of stixels within one spatial modulation period d. Since the stixel size of the metasurface is fixed ($d_0 = \lambda_0/5$), the total spatial period $d = Nd_0$ can be controlled by changing the path number N. This impresses a modulation wave number $\beta_p = 2\pi/d = 2\pi/(N\lambda_0/5)$ onto the metasurface. N adjacent stixels are modulated with bias signals staggered in time by an interval T_p/N, where $T_p = 1/f_p$ is the temporal-modulation period. In other words, the capacitance modulation of the metasurface satisfies the following

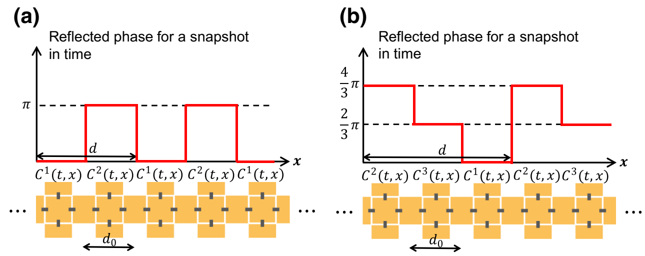

FIG. 5. Modulation scheme for the SDTWM metasurface. The stixel (unit-cell) dimension is $d_0 = 6$ mm and the spatial-modulation period is $d = Nd_0$. (a) A two-path modulation scheme ($d = 2d_0$). (b) A three-path modulation scheme ($d = 3d_0$).

relationship:

$$C(t,x) = C\left(t - \frac{T_p}{N}, x - \frac{d}{N}\right). \tag{5}$$

The spatial variation across one stixel is approximated to be uniform. Examples of two- and three-path spatiotemporal-modulation schemes are shown in Fig. 5. At any given time, the spatial variation of the reflection phase is a discretized sawtooth (blazed grating) ranging from 0 to approximately 2π over a period $d = Nd_0$. In this paper, the capacitance modulation on each stixel is chosen to either produce a sawtooth or sinusoidal reflection phase with respect to time. The procedure for obtaining the capacitance modulation based on the desired reflection phase is outlined within Supplemental Material I [48]. An example is shown in Fig. 6, where each stixel generates a staggered sawtooth reflection phase in time.

As mentioned, one can view each column of stixels as a path in a N-path network. In contrast to an N-path

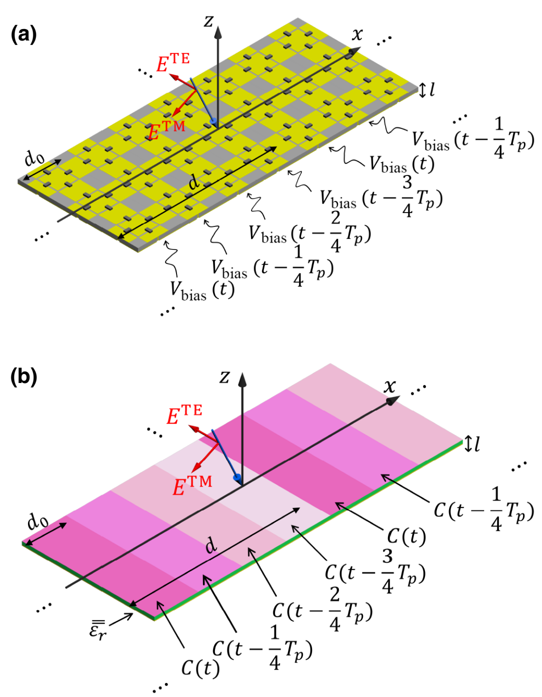

FIG. 4. Modulation scheme of the SDTWM metasurface. (a) The designed metasurface with a SDTWM bias. The stixel size is $d_0 = 6$ mm and the spatial-modulation period is d. (b) Homogenized model of the SDTWM metasurface. The substrate is modeled as a uniaxial, anisotropic material.

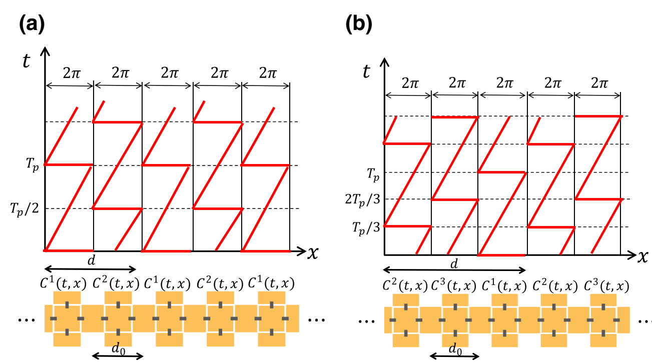

FIG. 6. Space-time modulation scheme for the SDTWM metasurface. The temporal modulation on each path is chosen to generate a sawtooth reflection phase varying from 0 to 2π over each period. The N adjacent paths of the metasurface are modulated by bias signals staggered in time by T_p/N. (a) A two-path modulation scheme ($d = 2d_0$). (b) A three-path modulation scheme ($d = 3d_0$).

circuit, the paths (columns of stixels) are not connected to a common input and output. Instead, each path is displaced by a subwavelength distance $d_0 = 6$ mm ($d_0 = \lambda_0/5$) from its adjacent paths. The N-path symmetry of the SDTWM metasurface establishes an interpath relation between the fields on adjacent paths [43]. Accounting for the incident tangential wave number, the total electric field on the metasurface must satisfy

$$E(t,x,y,z) = e^{j(\omega_0 T_p/N - k_x d/N)} E\left(t - \frac{T_p}{N}, x - \frac{d}{N}, y, z\right), \tag{6}$$

where ω_0 is the radial frequency of the incident wave, and k_x is the tangential wave number of the incident wave.

C. Modified Floquet expansion of SDTWM metasurfaces

For any space-time-modulated waveform, the capacitance modulation on the metasurface can be expanded as a double Floquet expansion in space and time [23],

$$C(t,x) = \sum_{m=-\infty}^{\infty} \sum_{q=-\infty}^{\infty} C_{mq} e^{-jm\beta_p x} e^{jq\omega_p t}, \tag{7}$$

where $\omega_p = 2\pi/T_p$ is the radial frequency (temporal-modulation wave number) of the modulation. Applying the capacitance relationship given by Eq. (5) to the double Floquet expansion in Eq. (7) reveals that the only nonzero values for coefficient C_{mq} are with $m = q + rN, r \in \mathbb{Z}$ (see Supplemental Material II [48]). This allows the capacitance expansion to be recast as the modified Floquet expansion,

$$C(t,x) = \sum_{r=-\infty}^{\infty} \sum_{q=-\infty}^{\infty} C_{rq} e^{jq(\omega_p t - \beta_p x)} e^{-jr\beta_d x}, \tag{8}$$

where $\beta_p = 2\pi/d$ is the modulation wave number, and $\beta_d = 2\pi/d_0 = N\beta_p$ is an additional wave number, which results from the discretization of the spatial modulation into stixels (paths). The summation over r accounts for the discontinuity in capacitance at the the boundary of each path as well as the microscopic variation of capacitance within the paths (which in this case is uniform). The summation over q accounts for the macroscopic capacitance variation over one spatial-modulation period d.

Similarly substituting a double Floquet expansion of the field into interpath relation given by Eq. (6) reveals that the total tangential field distribution above the metasurface can also be expressed in terms of the modified Floquet expansion,

$$E_t(t,x) = \sum_{r=-\infty}^{\infty} \sum_{q=-\infty}^{\infty} V_{rq} e^{-jr\beta_d x} e^{jq(\omega_p t - \beta_p x)} e^{j(\omega_0 t - k_x x)}. \tag{9}$$

The spatiotemporal harmonic pair (r, q) of the electromagnetic field has a tangential wave number

$$\begin{aligned} k_{xrq} &= q\beta_p + r\beta_d + k_x \\ &= (q + rN)\beta_p + k_x, \end{aligned} \tag{10}$$

and a corresponding radial frequency

$$\omega_{rq} = \omega_0 + q\omega_p. \tag{11}$$

This implies that the qth frequency harmonic, $\omega_0 + q\omega_p$, of the field is associated with an infinite number of spatial harmonics, which arise from the spatially discrete stixels. The reflected angle of each scattered harmonic pair is equal to

$$\theta_{rq} = \arcsin \frac{k_{xrq}}{\omega_{rq}/c} = \arcsin \frac{[(q + rN)\beta_p + k_0 \sin\theta_i]}{\omega_{rq}/c}. \tag{12}$$

Compared to the standard double Floquet expansion in Eq. (7), the inclusion of the interpath relation significantly reduces the number of unknowns. It also reveals the underlying physics associated with the SDTWM system. In fact, Eq. (9) allows one to separate the field into its macroscopic and microscopic variation. In addition, the field expansion in Eq. (9) indicates that unique physical phenomena, such as subharmonic mixing, can be achieved by a SDTWM metasurface, much like in an N-path circuit. Subharmonic mixing occurs when the spatial-modulation period of the metasurface is electrically small, which we discuss in detail in Sec. III B.

D. Scattered-field calculation of SDTWM metasurfaces

The scattered field of the SDTWM metasurface for an oblique, monochromatic incident wave can be solved using the boundary condition at $z = 0$,

$$H_t|_{z=0^+} - H_t|_{z=0^-} = \frac{d}{dt}[C(t,x)E_t]. \tag{13}$$

The space-time tangential fields as well as the capacitance modulation can be expressed in the form of the modified Floquet expansion given by Eqs. (8) and (9). In addition, we can separate the total tangential field on the metasurface

($z = 0^+$) into incident and reflected tangential fields,

$$E_t^{\rm inc} = V_{00}^{\rm inc} e^{j(\omega_0 t - k_x x)}, \tag{14}$$

$$E_t^{\rm ref} = \sum_{r,q=-\infty}^{\infty} V_{rq}^{\rm ref} e^{-jr\beta_d x} e^{jq(\omega_p t - \beta_p x)} e^{j(\omega_0 t - k_x x)}. \tag{15}$$

To solve for the scattered field, the incident and reflected space-time harmonics are organized into vectors as $\mathbf{V}^{\rm inc}$ and $\mathbf{V}^{\rm ref}$ respectively. Each entry corresponds to a unique spatiotemporal harmonic pair (r, q). The vector $\mathbf{V}^{\rm inc}$ contains only a single entry since the incident field is a monochromatic plane wave. Based on the detailed derivation in Supplemental Material III [48], the reflected electric field can be calculated for each polarization [25],

$$\mathbf{V}^{\rm ref} = (\mathbf{Y}^{\rm TX} + \mathbf{Y}_0^{\rm TX})^{-1}(\mathbf{Y}_0^{\rm TX} - \mathbf{Y}^{\rm TX})\mathbf{V}^{\rm inc}, \tag{16}$$

where the superscript "X" is "E" for TE-polarized waves and "M" for TM-polarized waves. $\mathbf{Y}_0^{\rm TX}$ is the free-space tangential wave admittance matrix. It is a diagonal matrix containing entries of the free-space admittances at the corresponding frequency harmonics. $\mathbf{Y}^{\rm TX}$ is the input admittance matrix of the time-modulated metasurface. It is not a diagonal matrix since the space-time-modulated capacitive sheet introduces coupling between different harmonic pairs.

III. THREE OPERATING REGIMES OF A SDTWM METASURFACE

As mentioned earlier, the modified Floquet expansion given by Eq. (9) separates the field into macroscopic and microscopic spatial variations. It is clear that when the number of stixels within a spatial period (the path number N) increases, the field variation across one stixel decreases. As a result, the microscopic spatial variations on the metasurface will decrease. On the other hand, when the number of stixels within a spatial period is small, the microscopic spatial variation dominates. This enables the same SDTWM metasurface to achieve different functions depending on the spatial-modulation period d. In fact, the electromagnetic behavior of the metasurface can be categorized into three regimes.

In this section, we discuss the scattering performance of the SDTWM metasurface, for electrically small, large, and wavelength-scale spatial-modulation periods. In addition, scattering for temporal modulation only (one path, $N = 1$) is given in Sec. III A as reference, since it represents the limiting case where the modulation period approaches infinity. Computed results are given in this section for various space-time modulation examples in the three regimes. For convenience, the conversion loss and sideband suppression at the prescribed observation angle are provided in Table I, for each of the examples that follow. The table is referred to throughout this section. In all of the examples studied, the incident signal frequency is $f_0 = 10$ GHz. The modulation frequency, $f_p = 25$ kHz, which is the maximum frequency that can be experimentally validated using the multichannel digital-to-analog converters available to the authors (see Sec. IV). For each angle of incidence, the capacitance modulation is calculated based on Eq. (S.4) within the Supplemental Material [48] to achieve the desired time-varying reflection phase. Unless specifically stated otherwise, the reflection phase of each stixel (path) is a sawtooth function in time. For both polarizations, the field is expanded into 141×141 (r, q) harmonic pairs. The temporal capacitance modulation on each path is truncated to 101 temporal harmonics.

A. Temporal modulation ($\beta_p = 0$): serrodyne frequency translation

It is instructive to first consider the behavior of the metasurface when it is uniformly biased across all stixels. In

TABLE I. Simulated conversion loss and sideband suppression for desired reflected frequency harmonic f' given: N, the path number; θ_i, the incident angle; $\theta_{\rm obs}$, the observation angle, and the temporal phase modulation waveform (either a sawtooth or a sinusoid). Note that positive values of θ_i and $\theta_{\rm obs}$ correspond to waves traveling along the positive x direction.

Ex.	N	θ_i	$\theta_{\rm obs}$	Waveform	f'	Conversion loss (dB)		Sideband suppression (dB)	
						TE	TM	TE	TM
0	1	25°	25°	saw	$f_0 + f_p$	0.11	0.13	22.83	21.64
1	2	25°	25°	saw	$f_0 + 2f_p$	0.34	0.50	17.32	13.19
2	3	25°	25°	saw	$f_0 + 3f_p$	0.45	0.87	14.14	10.46
3	20	25°	42°	saw	$f_0 + f_p$	0.13	0.62	22.83	11.75
4	20	−42°	−25°	saw	$f_0 + f_p$	0.13	0.62	24.17	9.04
5	20	−7.2°	7.2°	saw	$f_0 + f_p$	0.12	0.23	23.01	19.58
6	4	39°	−39°	saw	$f_0 + 3f_p$	2.24	1.45	9.59	11.69
7	4	−39°	39°	saw	$f_0 + f_p$	1.24	0.95	10.63	11.89
8	4	39°	−39°	sin	$f_0 - f_p$	0.50	0.31	14.94	17.71
9	4	−39°	39°	sin	$f_0 + f_p$	0.49	0.31	14.95	17.65

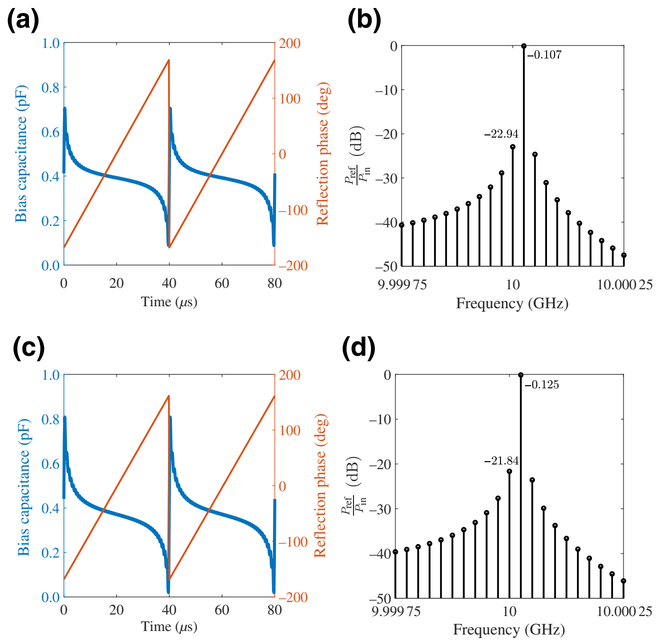

FIG. 7. (a) Calculated capacitance modulation of the time-modulated metasurface for TE polarization. (b) Analytical reflection spectrum of the homogenized, lossless, time-modulated metasurface for TE polarization. (c) Calculated capacitance modulation of the time-modulated metasurface for TM polarization. (d) Analytical reflection spectrum of the homogenized, lossless, time-modulated metasurface for TM polarization.

this case, there is no spatial variation in the homogenized model and the reflected power spreads into discrete frequency harmonics due to the periodic time variation of the reflection phase.

Suppose the reflection phase is modulated by a sawtooth waveform. In this case, serrodyne frequency translation is expected [15]. The incident wave is assumed to impinge on the metasurface at an oblique angle of 25°. The capacitance modulation needed to upconvert the wave to $f_0 + f_p$ is calculated within Supplemental Material I [48], and shown in Fig. 7 for each polarization. The reflected spectra for the two orthogonal polarizations (shown in Fig. 7) clearly show a Doppler shift to a frequency of $f_0 + f_p$. For each polarization, the conversion loss and sideband suppression are provided in example 0 of Table I. As mentioned earlier, the equivalent circuit model of the unit cell provides a phase range that is slightly less that 2π (1.6π for TE polarization and 1.54π for TM polarization used in the analysis), resulting in undesired sidebands. For TM polarization, the reflection phase range is slightly less than for TE at the oblique angle of 25°, resulting in a slightly higher conversion loss.

B. Small spatial-modulation period ($|k_x \pm \beta_p| > k_0$)

In this section, we consider a spatial-modulation period d that is electrically small (N is small). In this case, the

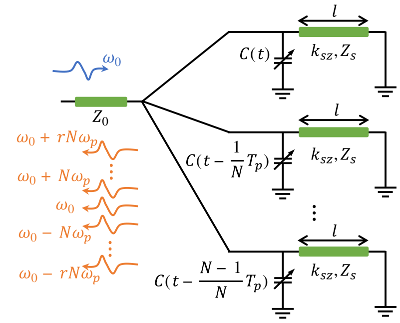

FIG. 8. Equivalent circuit model of the SDTWM metasurface when the spatial-modulation period is much smaller than the wavelength of radiation.

paths can be viewed as collocated and a N-path circuit model can be used to approximate the physical structure. The equivalent circuit model of the spatiotemporally modulated metasurface for $d \ll \lambda_0$ is depicted in Fig. 8. Since the time variation of each path is staggered, certain harmonics mixing products are suppressed in the reflected signal, allowing subharmonic mixing.

Another way of understanding the subharmonic mixing behavior of the metasurface is depicted in Fig. 9(a). If the modulation period d of the SDTWM metasurface is electrically small ($|k_x \pm \beta_p| > k_0$), then both the $+1$ ($k_x + \beta_p$) and -1 ($k_x - \beta_p$) spatial harmonics are outside of the light cone. The large modulation wave number β_p in this regime can lead to a number of higher-order harmonics existing outside the light cone. In this case, the metasurface can convert an incident wave to a surface wave, provided that the corresponding surface wave is supported by the metasurface. However, when the corresponding surface wave is not supported, the power can only couple to radiating harmonics: those within the light cone. Based on Eq. (10), the radiating harmonics are those with

$$q + rN = 0. \tag{17}$$

Since $r \in \mathbb{Z}$, Eq. (17) implies that propagating harmonics correspond to $q = 0, \pm N, \pm 2N \ldots$. Therefore, the radiated reflected wave only contains frequency harmonics at $f_0 +$

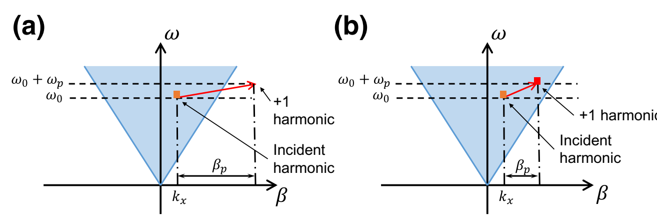

FIG. 9. Graphic representation of the spatial and temporal frequency shifts for different modulation wave numbers. (a) The modulation wave number β_p is large. (b) The modulation wave number β_p is small.

rNf_p, where $r \in \mathbb{Z}$. As a result, the metasurface can achieve subharmonic frequency translation.

More generally, for harmonic pairs with tangential wave numbers larger than free space ($k_{xrq} > \omega_{rq}/c$), the transverse resonance condition can be used to judge if the corresponding surface waves are supported by the SDTWM metasurface.

$$\det\left(\mathbf{Y}^{\mathbf{TX}} + \mathbf{Y}_{\mathbf{0}}^{\mathbf{TX}}\right) = 0, \tag{18}$$

Solving Eq. (18) yields the $\omega_0 - k_x$ dispersion relationship for the supported surface wave. Note that when a surface wave is supported, the reflection coefficient $V_{\text{ref}}/V_{\text{inc}}$ in Eq. (16) diverges. This is not the case for the incident angle and path number N combinations considered in this paper. Thus, for all the proceeding examples presented in this paper, a surface wave is not supported by the metasurface.

Note that, the subharmonic mixing phenomena can only be observed when the spatial discretization of the metasurface is considered. In the continuum limit, subwavelength spatial modulation results in specular reflection at the same frequency as the incident wave. However, the spatial discretization introduces additional spatial harmonics [the summation over r in (9) that can couple to the incident wave]. In addition, all the reflected propagating harmonics share the same tangential wave number as the incident wave (since $k_{xrq} = k_x$, when $q + Nr = 0$). Since the modulation frequency (25 KHz) is much lower than the incident frequency (10 GHz), $f_p \ll f_0$, all the harmonics are at a reflection angle of 25°, as depicted in Fig. 10. If the modulation frequency f_p is comparable with f_0, then each of the reflected, propagating frequency harmonics will have different radiated angles due to their substantially different free-space wave numbers.

With the capacitance modulation shown in Figs. 7(a) and 7(c), the sawtooth reflection phase on each path enables the metasurface to upconvert the frequency to the first propagating frequency harmonic. In this case, the metasurface performs subharmonic frequency translation from f_0 to $f_0 + Nf_p$. Since the stixel size of the presented metasurface is fixed to $d_0 = \lambda_0/5$, examples of two- and three-path modulation ($N = 2, 3$) are chosen to satisfy the small period condition ($|k_x \pm \beta_p| > k_0$). The incident wave impinges on the metasurface with an oblique angle of 25°. The computed reflection spectra for both

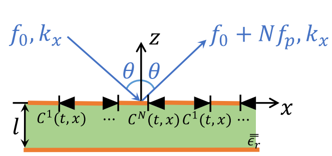

FIG. 10. Specular subharmonic frequency translation of the SDTWM metasurface. For the presented metasurface, this can be achieved when $N = 2$ or 3.

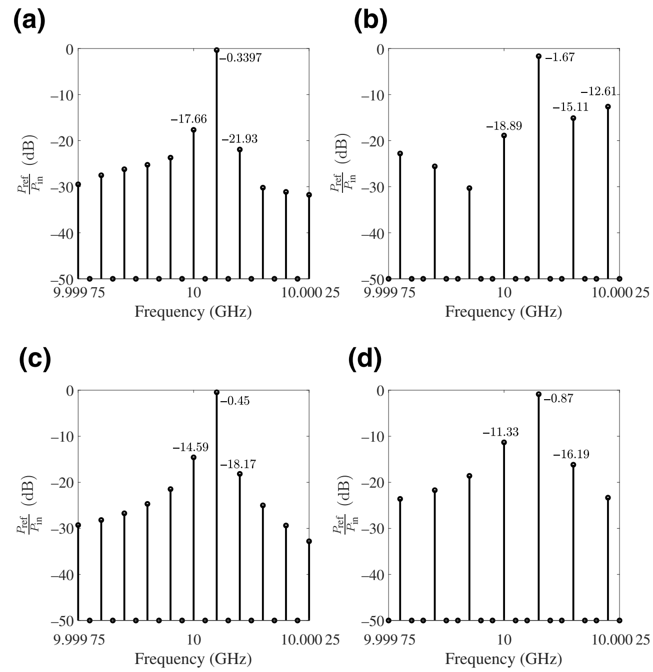

FIG. 11. Theoretical reflection spectrum of the homogenized, lossless, SDTWM metasurface. (a) Two-path ($N = 2$) modulation for TE polarization. (b) Three-path ($N = 3$) modulation for TE polarization. (c) Two-path ($N = 2$) modulation for TM polarization. (d) Three-path ($N = 3$) modulation for TM polarization.

polarizations are shown in Fig. 11, which clearly demonstrate subharmonic frequency translation. The reflected harmonics are only radiated at $f = f + rNf_s$ with $r \in \mathbb{Z}$. Doppler-like frequency translations are observed for both polarizations, where the dominant propagating reflected wave is at frequency $f_0 + Nf_p$. The conversion loss and sideband suppression for both polarizations using two-path and three-path modulation are provided in examples 1 and 2 of Table I.

As mentioned earlier, each stixel provides a phase range that is slightly smaller than 2π, resulting in conversion loss and undesired sidebands. It can be seen that, as the converted frequency harmonic (which is equal to the path number N in this case) is increased, the conversion loss increases and the sideband suppression decreases. This is because the N-path metasurface up-converts the frequency to the first propagating harmonic pair. The higher the up-converted frequency, the longer this process takes and the larger the conversion loss due to the formation of sidebands that results from the imperfect reflection phase range.

C. Large spatial-modulation period ($|k_x \pm \beta_p| < k_0$)

When the modulation period d is electrically large (N is large), the spatial-modulation wave number β_p is small, as depicted in Fig. 9(b). In this operating regime, both the +1 ($k_x + \beta_p$) and −1 ($k_x - \beta_p$) spatial harmonics are inside the light cone. When N is a very large value, the stixel size can be seen as infinitesimally small compared to the spatial-modulation period ($d_0 \ll d$). As a result, the discontinuity in the capacitance of neighboring stixels vanishes and the modulation can be approximated as a continuous function of space. According to Eq. (8), the capacitance coefficient C_{rq} is zero for $r \neq 0$. For this case, the field variation across each stixel is small, and the capacitance-modulation waveform is simplified to the continuum limit:

$$C(t,x) = \sum_{q=-\infty}^{\infty} C_q e^{jq(\omega_p t - \beta_p x)}. \tag{19}$$

Note that Eq. (19) is of the form of a traveling wave, $C(t,x) = C(t - x/v_p)$, where $v_p = \omega_p/\beta_p$. For such a modulation, the metasurface supports harmonics at frequency $f_0 + qf_p$, with a corresponding wave number $k_x + q\beta_p$. In other words, the SDTWM metasurface with large spatial-modulation period shows a similar performance to a continuous traveling-wave-modulated structure. Serrodyne frequency translation to a deflected angle can be achieved using the sawtooth waveform given in Fig. 7.

Let us consider the example shown in Fig. 12(a), where a wave is incident at an angle $\theta_1 = 25^\circ$ and the number of paths is large, $N = 20$. From Eq. (10), the tangential wave numbers of the reflected harmonic pairs are given by

$$\begin{aligned} k_{xrq}\big|_{r=0} &= q\beta_p + k_0 \sin(25^\circ) \\ &= \frac{q}{4}k_0 + k_0 \sin(25^\circ), \end{aligned} \tag{20}$$

given that $d = 20d_0 = 4\lambda_0$. The harmonics located inside the light cone (propagating harmonics) are those with $q = 0, \pm 1, \pm 2, -3, -4, -5$. For the capacitance variation shown in Figs. 7(a) and 7(c), the metasurface acts as a serrodyne frequency translator. It upconverts the incident wave to the harmonic pair $(r = 0, q = 1)$ with frequency $f = f_0 + f_p$. In this case, each scattered harmonic has its own tangential wave number, and thus reflects to a different angle given by Eq. (12). The strongest harmonic $(f_0 + f_p)$ reflects to $\theta_2 = 42^\circ$, as shown in Fig. 12(a). The reflected spectra for both polarizations are given in Fig. 13.

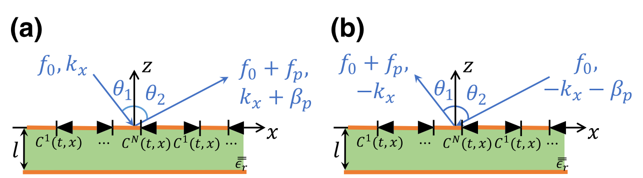

FIG. 12. The SDTWM metasurface performing serrodyne frequency translation to a deflected angle. The path number $N > 5$. The modulation frequency f_p is much lower than the incident frequency f_0. (a) Wave is incident at an oblique angle θ_1. (b) Wave is incident at an oblique angle $-\theta_2$.

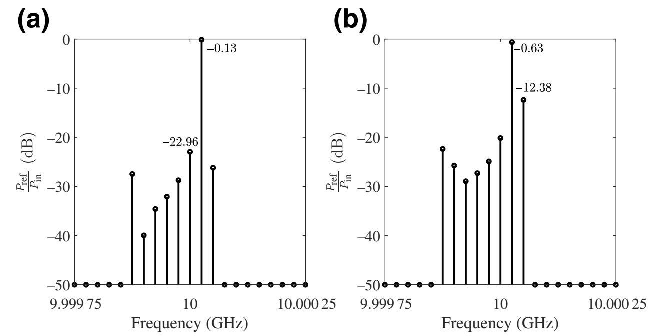

FIG. 13. Theoretical reflection spectrum of the homogenized, lossless, SDTWM metasurface with an incident angle of 25°. (a) 20-path ($N = 20$) modulation for TE polarization. (b) 20-path ($N = 20$) modulation for TM polarization.

The conversion loss and sideband suppression for both polarizations are provided in example 3 of Table I.

Let us consider another example [shown in Fig. 12(b)] where the spatiotemporal modulation of the metasurface and incident frequency are kept the same, but the incident and reflected angles are swapped. The incident angle is $\theta_2 = -42^\circ$. Each scattered harmonic pair of the reflected field has tangential wave number

$$k_{xrq}\big|_{r=0} = \frac{q}{4}k_0 - k_0 \sin(42^\circ). \tag{21}$$

where $q = 0, \pm 1, 2, 3, 4, 5, 6$. The metasurface frequency translates the incident signal at f_0 to the harmonic pair $(r = 0, q = 1)$, which is at frequency $f = f_0 + f_p$. The tangential wave number of the harmonic pair $(r = 0, q = 1)$ can be easily calculated as $-k_0 \sin(25^\circ)$. When modulation frequency f_p is comparable to incident frequency f_0, the reflection angle can differ from $\theta_1 = -25^\circ$ due to the significant change in the free-space wave number at the reflected frequency [17], as shown within Supplemental Material IV [48]. However, modulation frequency here is $f_p = 25$ kHz, which is far smaller than the incident frequency of $f_0 = 10$ GHz. As a result, the reflection angle is -25°. The reflection spectra for both polarizations are given in Fig. 14. From example 4 of Table I, it can be seen that the conversion loss and sideband suppression are practically identical to those of the previous example (shown in example 3 of Table I).

Furthermore, in this regime of large spatial-modulation period, the incident angle can be chosen to achieve retroreflection. According to Eq. (12), setting $\theta_{rq} = -\theta_i$ yields an expression for the incidence angles at which retroreflection occurs for the converted spatiotemporal harmonic. For this case, the modulation wave number $\beta_p = 2k_x$, as shown in Fig. 15. The reflected wave propagates back to the source with an up-converted frequency. The retroreflection angle

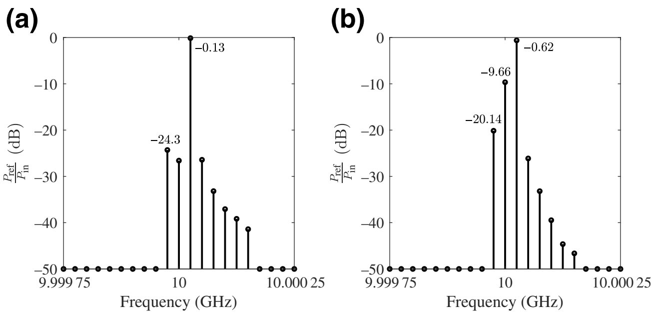

FIG. 14. Theoretical reflection spectrum of the homogenized, lossless, SDTWM metasurface with an incident angle of −42°. (a) 20-path ($N = 20$) modulation for TE polarization. (b) 20-path ($N = 20$) modulation for TM polarization.

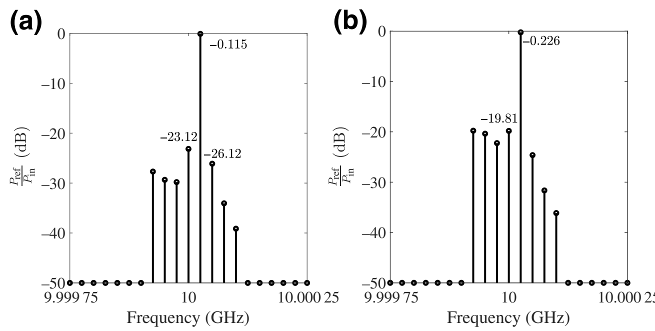

FIG. 16. Theoretical reflection spectrum of the homogenized, lossless, SDTWM metasurface for an incident angle of 7.18°. (a) 20-path ($N = 20$) modulation for TE polarization. (b) 20-path ($N = 20$) modulation for TM polarization.

θ_i can be calculated by solving $\theta_{0,1} = -\theta_i$ in Eq. (12),

$$\theta_i = -\arcsin\frac{\beta_p}{2k_0} = -\arcsin\frac{\lambda_0}{2Nd_0}. \tag{22}$$

Here, the number of paths is chosen to be $N = 20$, and the retroreflection angle is calculated to be $\theta_i = -7.18°$. The calculated reflection spectra for both polarizations are shown in Fig. 16. The spectra clearly show a Doppler shift to frequency $f_0 + f_p$. The conversion loss and sideband suppression for both polarizations are provided in example 5 of Table I. Note that in Fig. 16, only the harmonic pair ($r = 0, q = 1$) (at frequency $f_0 + f_p$) is retroreflective. The reflection angle of other harmonics can be calculated based on Eq. (12).

D. Wavelength-scale spatial-modulation period ($|k_x| + |\beta_p| > k_0$ and $||k_x| - |\beta_p|| < k_0$)

In this section, we consider a spatial-modulation period that is on the order of the wavelength of radiation ($|k_x| + |\beta_p| > k_0$ and $||k_x| - |\beta_p|| < k_0$). In this regime, either the +1 ($k_x + \beta_p$) or the −1 ($k_x - \beta_p$) spatial harmonic is inside the light cone, as shown in Fig. 17. For the fixed stixel size of $d_0 = \lambda_0/5$, four-path modulation ($N = 4$) is chosen to satisfy the wavelength-scale period condition. In this regime, the SDTWM metasurface allows both small and large period electromagnetic effects. That is, both subharmonic mixing and angular deflection can be simultaneously achieved. In this section, the deflective and retroreflective behavior of the metasurface is showcased for various scenarios. In the first case, the metasurface exhibits simultaneous subharmonic frequency translation and deflection. The incident angle is specifically chosen to achieve subharmonic frequency translation in retroreflection. In the second case, we show that the retroreflective frequency can be switched by changing the temporal-phase modulation waveform to sinusoidal.

1. Deflective and retroreflective subharmonic frequency translation

First, let us consider the example shown in Fig. 17(a), where a wave is incident on the metasurface with a positive k_x value. According to Eq. (10), the radiated harmonics are those with

$$q + rN = 0 \quad \text{or} \quad q + rN = -1. \tag{23}$$

Equation (23) implies that the radiated reflected wave contains frequency harmonics at $f_0 + rNf_p$ and $f_0 + (rN - 1)f_p$, where $r \in \mathbb{Z}$. Under a capacitance variation that generates sawtooth reflection phase, the reflected wave is upconverted to the first radiated frequency harmonic, which in this case is the harmonic pair ($r = -1, q = 3$). Therefore, the reflected wave is Doppler shifted to a frequency

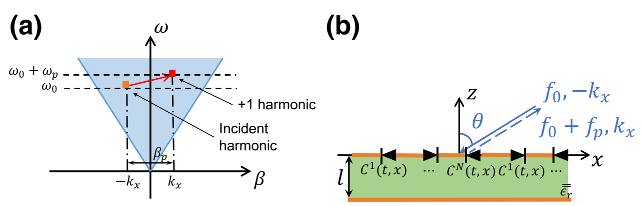

FIG. 15. (a) Graphic representation of the spatial and temporal frequency shift for a relatively large path number N. (b) Corresponding retroreflection performance for a relatively large path number N.

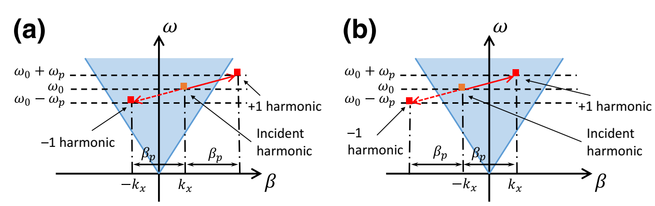

FIG. 17. Graphic representation of the spatial and temporal frequency shifts for a path number $N = 4$. (a) The incident tangential wave number k_x is positive. (b) The incident tangential wave number k_x is negative.

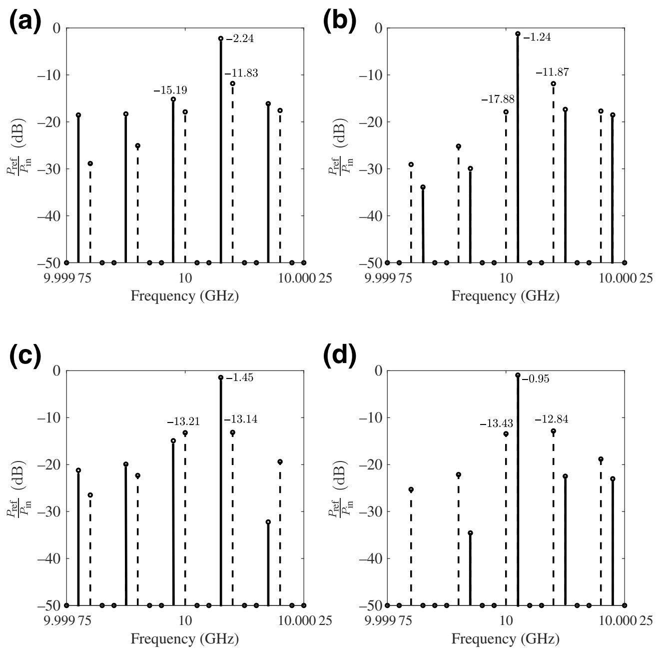

FIG. 18. Theoretical retroreflection spectrum of the homogenized, lossless, SDTWM metasurface. The harmonics denoted by solid lines retroreflect. The harmonics denoted by the dashed lines reflect in the specular direction. (a) Four-path ($N=4$) modulation for TE polarization for an incident angle of 39°. (b) Four-path ($N=4$) modulation for TE polarization for an incident angle of −39°. (c) Four-path ($N=4$) modulation for TM polarization for an incident angle of 39°. (d) Four-path ($N=4$) modulation for TM polarization for an incident angle of −39°.

f_0+3f_p. In addition, an incident angle is chosen such that the wave is retroreflected: $\beta_p=2k_x$ [see Fig. 17(a)]. The retroreflection angle can be calculated by setting $\theta_{-1,3}=-\theta_i$ in Eq. (12), which is 39° for a path number of $N=4$.

The calculated retroreflection spectra are shown in Figs. 18(a) and 18(c). Doppler-like frequency translation to frequency f_0+3f_p occurs for the incident angle of 39°, for both polarizations. In addition, the signal at f_0+3f_p is retroreflected. The conversion loss and sideband suppression for both polarizations are provided in example 6 of Table I. Note that in Figs. 18(a) and 18(c), only the harmonics represented by a solid line are retroreflected. The harmonics represented by dashed lines are reflected in the specular direction.

With a wavelength-scale spatial-modulation period, the performance of the metasurface is direction dependent. When the incident angle is −39°, as shown in Fig. 17(b), it is clear that the radiated harmonics are those with

$$q+rN=0 \quad \text{or} \quad q+rN=1. \tag{24}$$

In this case, the harmonic pair ($q=1,r=0$) is inside the light cone. Therefore, the metasurface performs serrodyne frequency translation: up-conversion to a frequency f_0+f_p. Since $\beta_p=2k_x$, the frequency of interest f_0+f_p is also retroreflected. The calculated reflection spectra are shown in Figs. 18(b) and 18(d). Doppler-like frequency translation to frequency f_0+f_p is observed for both polarizations. The conversion loss and sideband suppression for both polarizations are provided in example 7 of Table I. An illustration of the direction-dependent retroreflective behavior of the metasurface, with a wavelength-scale spatial-modulation period, is depicted in Fig. 19(a).

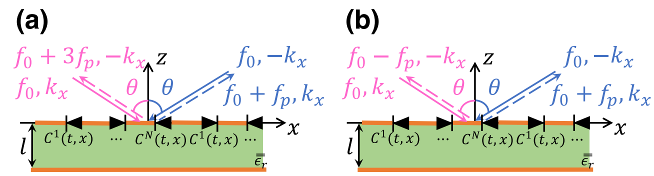

FIG. 19. Retroreflective performance of the SDTWM metasurface. The path number is $N=4$, and the retroreflection angle is $\theta=39°$. (a) The sheet capacitance generates a reflection phase on each column that is a sawtooth with respect to time. (b) The capacitance modulation on each column generates sinusoidal reflection phase with respect to time.

2. Retroreflective frequency translation with a staggered sinusoidal reflection phase

Here, retroreflection is achieved using stixels that generate staggered sinusoidal reflection phase with respect to time. The capacitance modulation waveform is shown in Figs. 20(a) and 20(c) for each polarization. When all the columns of the metasurface are homogeneously biased with the same waveform, the reflection spectra take the form of a Bessel function, as shown in Figs. 20(b) and 20(d). The reflection phase range is chosen to be 276° to suppress the zeroth harmonic in reflection [30]. Unlike the sawtooth modulation, the sinusoidal reflection phase excites both +1 ($r=0,q=1$) and −1 ($r=0,q=-1$) frequency harmonics.

Figure 17 shows that for a positive k_x incident wave number, the reflected +1 frequency harmonic is outside of the light cone ($|k_x+\beta_p|>k_0$), and the refleted −1 frequency harmonic is inside the light cone ($|k_x-\beta_p|<k_0$). Since the +1 frequency harmonic does not radiate and is not supported by the metasurface as a surface wave, the power is reflected from the metasurface with a frequency of f_0-f_p. In other words, for a wavelength-scale spatial-modulation period, the metasurface supports single-sideband frequency translation with the sinusoidal modulation.

When the incident angle is 39°, the frequency of interest f_0-f_p is retroreflective. Again, the retroreflective behavior of the metasurface is directionally dependent. When the incident angle is −39°, the +1 frequency harmonic is inside the light cone. The retroreflected wave is radiated at a frequency f_0+f_p. For this case, the direction-dependent retroreflective behavior of the metasurface is depicted in

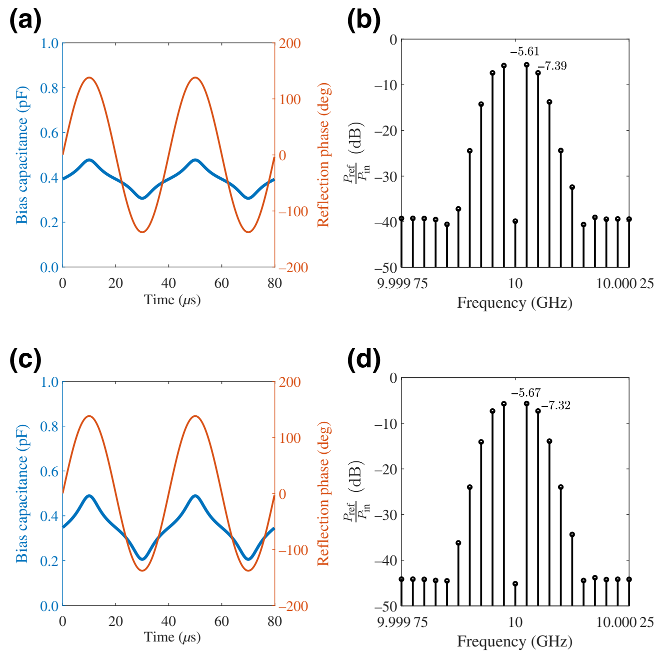

FIG. 20. (a) Calculated capacitance modulation for a sinusoidal reflection phase versus time for TE polarization. (b) Analytical reflection spectrum of the homogenized, lossless time-modulated metasurface for TE polarization. (c) Calculated capacitance modulation for a sinusoidal reflection phase versus time for TM polarization. (d) Analytical reflection spectrum of the homogenized lossless time-modulated metasurface for TM polarization.

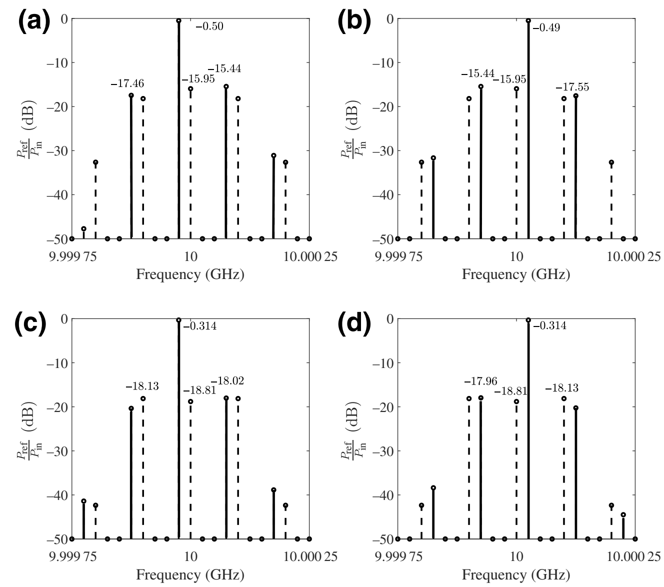

FIG. 21. Analytical retroreflection spectrum of the homogenized, lossless, SDTWM metasurface. The capacitance modulation generates a sinusoidal reflection phase on each path. The harmonics denoted by the solid lines are propagating in the retroreflective direction. The harmonics denoted by the dashed lines are propagating in specular direction. (a) Four-path ($N = 4$) modulation for TE polarization for an incident angle of 39°. (b) Four-path ($N = 4$) modulation for TE polarization for an incident angle of −39°. (c) Four-path ($N = 4$) modulation for TM polarization for an incident angle of 39°. (d) Four-path ($N = 4$) modulation for TM polarization for an incident angle of −39°.

Fig. 19(b). The calculated reflection spectra are shown in Fig. 21. As expected, Doppler-like frequency translation to $f_0 - f_p$ is observed for an incident angle of 39°, and $f_0 + f_p$ for an incident angle of −39°. The conversion loss and sideband suppression for both polarizations are provided in examples 8 and 9 of Table I.

Note that the retroreflection angle for both of the two cases (with sawtooth and sinusoidal reflection phase) was ±39° for a path number of $N = 4$. By simply changing the temporal modulation waveform, the retroreflection frequency is changed from $f_0 - f_p$ to $f_0 + 3f_p$, for the same incident angle of 39°.

IV. EXPERIMENTAL REALIZATION OF A SDTWM METASURFACE

In this section, an experimental prototype of the SDTWM metasurface is developed for experimental verification. Details of the metasurface realization, as well as the measurement setup used to characterize its performance, are given in Sec. IV A. The static performance of the metasurface under various dc bias conditions is presented in Sec. IV B. Based on this static (dc) characterization, the required bias waveform to attain a particular desired time-dependent reflection phase is discussed in Sec. IV C. This section also includes the measured reflection spectra for time variation alone.

A. Metasurface design and measurement setup

A stixel (unit cell) of the dual-polarized metasurface is depicted in Fig. 2(a). Varactor diodes (MAVR-000120-1411 from MACOM [49]) are integrated onto the metasurface to act as tunable capacitances for two orthogonal polarizations. The biasing networks for both polarizations are printed behind the ground plane, as shown in Figs. 22(a) and 22(c). Each bias layer consists of 28 metallic lines that can independently modulate all 28 columns of the metasurface. A total of 3136 MAVR-000120-1411 varactor diodes are mounted onto the metasurface. The varactor diodes are biased through vias located in the center of the metallic patches. A photo of the fabricated metasurface is shown in Fig. 22(b). The metallic traces of the bias layers are routed to four D-SUB connectors edge mounted to the metasurface. Rogers 4003C ($\epsilon_r = 3.55$ and $\tan\delta = 0.0027$) substrate with a thickness of 0.508 mm is chosen for each layer. Rogers 4450F ($\epsilon_r = 3.52$ and $\tan\delta = 0.004$) bondply, with a thickness of 0.101 mm is used as an adhesive layer. A cross section of the material layers used to fabricate the metasurface is shown in Fig. 22(c). The

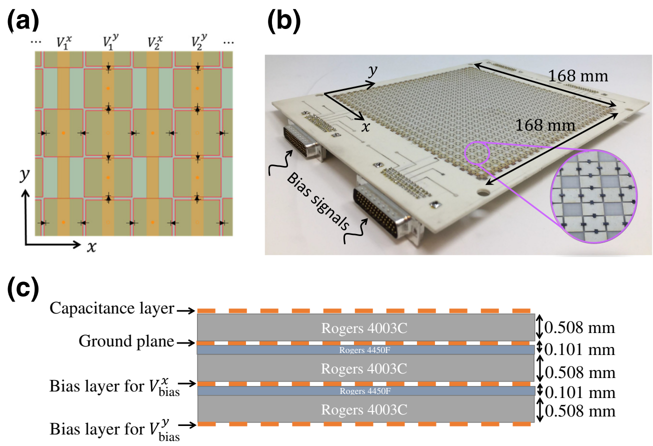

FIG. 22. (a) Transparent view of the metasurface prototype with two bias layers independently controlling each polarization. (b) Photograph of the fabricated metasurface. (c) Cross section of the fabricated metasurface.

total thickness of the fabricated metasurface is 1.726 mm (0.06λ).

The metasurface is experimentally characterized using the quasioptical Gaussian beam system shown in Fig. 23. In the experimental setup, the fabricated metasurface is illuminated by a spot-focusing lens antenna (SAQ-103039-90-S1). The antenna excites a Gaussian beam with a beamwidth of 50 mm at a focal length of 10 cm. The width of the fabricated metasurface is larger than 1.5 times the beamwidth to limit edge diffraction. A continuous-wave signal provided by an Anritsu MS4644B vector network analyzer at $f_0 = 10$ GHz is used as the incident signal. The amplitude of the incident signal impinging on the metasurface is measured to be −20 dBm. An Agilent E4446A spectrum analyzer is used to measure the reflected spectrum. The path loss of the system is measured and calibrated out of the measurements. The metasurface is modulated by four Keysight M9188A 16-channel D/A converters. Each channel of the D/A converter is synchronized and staggered in time. The D/A converter has an output voltage range from 0 to 30 V, and a maximum modulation frequency of $f_p = 25$ kHz.

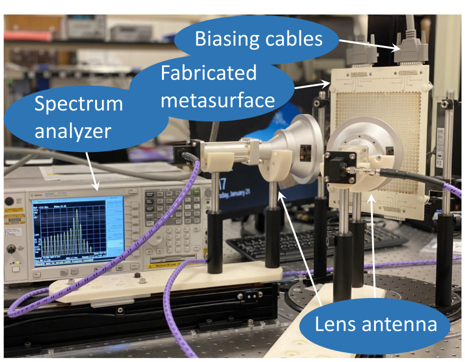

FIG. 23. Photograph of the quasi-optical, free-space measurement system.

B. Measurements of a dc-biased metasurface: tunable reflection phase

We first look at the simulated and measured dc performance of the metasurface prototype. The capacitance provided by the varactors ranges from 0.18 to 1.2 pF. Using the commercial electromagnetic solver Ansys HFSS, a full-wave simulation of the stixel (unit cell) shown in Fig. 2(a) is conducted in the absence of time variation. In the simulations, each varactor diode is modeled as a lumped capacitance in series with a resistance. The capacitance and resistance values of the varactor diode are extracted as a function of bias voltage from its SPICE model [49].

The simulated reflection coefficients of the metasurface for various varactor capacitance values are given in Fig. 24. The incident angle is set to 25°. At the operating frequency of 10 GHz, the reflection phase of the metasurface can be varied from −181.1° to 155° for TE polarization, providing a phase range of 336.1°. For TM polarization, the reflection phase of the metasurface can be varied from −181.8° to 146.3°, providing a phase range of 328.1°. At the operating frequency of 10 GHz, the simulated reflection amplitude for both polarizations remains greater than −3 dB across the entire phase range. Note that

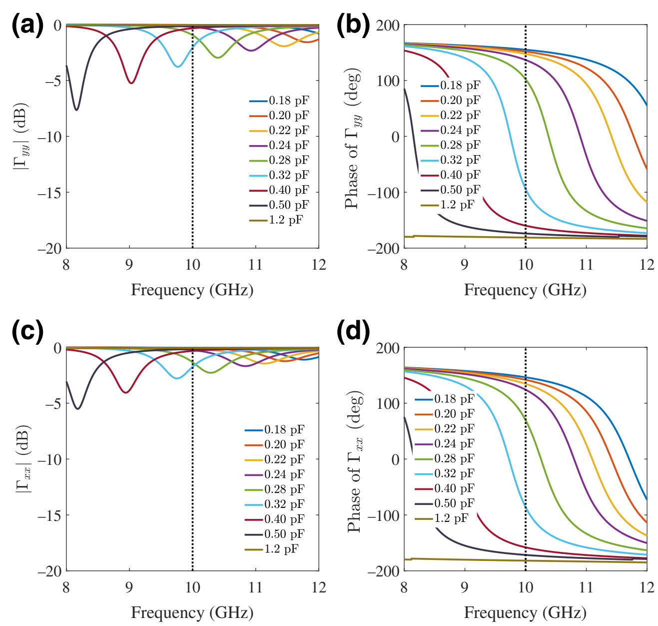

FIG. 24. Simulated reflection coefficient amplitude and phase of the realized metasurface for a range of varactor capacitances. The incident wave is obliquely incident at an angle of 25°. (a) Reflection amplitude for TE polarization. (b) Reflection phase for TE polarization. (c) Reflection amplitude for TM polarization. (d) Reflection phase for TM polarization.

at the resonant frequency of the unit cell, the input susceptance goes to zero, and the surface admittance becomes purely resistive. The effective resistance seen by the incident wave is determined by the losses within the dielectric, the finite conductivity of the metallic patches and the losses of the varactor. As a result, the reflection coefficient magnitude dips at the resonance frequency, and the reflection phase becomes zero (a high-impedance condition). The highest return loss at 10 GHz is 3.41 dB for TE polarization, for a varactor capacitance of 0.313 pF. For TM polarization, the highest return loss at 10 GHz is 2.47 dB, for a varactor capacitance of 0.30 pF. The metasurface incurs higher loss for TE polarization than TM polarization. This is because, at the incident angle of 25°, the value of the free-space tangential wave impedance for TE polarization is closer (impedance matches better) to the purely resistive input impedance of the metasurface at resonance. The simulated reflected cross-polarization of the metasurface is lower than −50 dB for all the orthogonal varactor capacitance variations.

The static (dc-biased) performance of the metasurface is measured under an oblique angle of 25°. The measured TE and TM reflection coefficients under various bias voltages are given in Fig. 25. The bias voltage used in measurement ranged from 0 to 15 V, providing a varactor capacitance range of 0.18 to 1.2 pF. At the operating frequency of 10 GHz, the measured reflection phase of the metasurface can be varied from −182.7° to 149.9° for TE polarization, corresponding to a phase range of 332.6°. For TM polarization, the measured reflection phase can be varied from −176.9° to 147.6°, corresponding to a phase range of 324.5°. At resonance, the measured reflection amplitude is found to be much lower than in simulation, indicating higher losses in the fabricated metasurface. This can be attributed to additional Ohmic loss within the diode as well as losses introduced by the tinning and soldering procedures used to mount the diodes. Nevertheless, the simulated and measured static performances of the metasurface are in good agreement. A detailed comparison between simulation and measurement for each bias voltage is given within the Supplemental Material V [48].

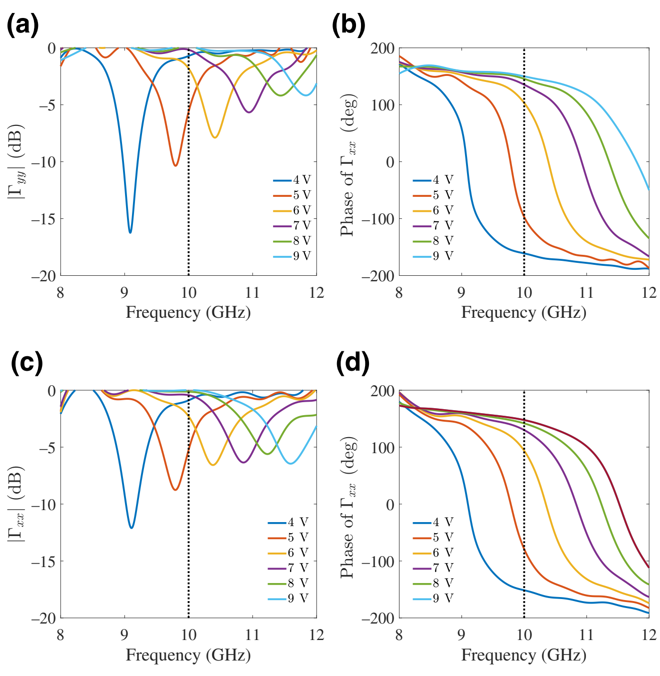

FIG. 25. Measured reflection coefficient amplitude and phase of the metasurface prototype for a range of bias voltages. The incident wave is oblique at an angle of 25°. (a) Reflection amplitude for TE polarization. (b) Reflection phase for TE polarization. (c) Reflection amplitude for TM polarization. (d) Reflection phase for TM polarization.

A harmonic balance simulation using the Keysight ADS circuit solver is used to verify the theoretical analysis and to compute the reflection spectrum. However, to use the harmonic balance circuit solver, a circuit equivalent of the fabricated metasurface needed to be extracted for each polarization from full-wave scattering simulations. A voltage-dependent resistance is added to it to account for the added losses observed in measurement. The equivalent circuits for the two polarizations under an oblique incident angle of 25° are given within Supplemental Material V [48]. From the equivalent circuits, the capacitance modulation required to obtain a given reflection phase versus time dependence can be obtained, as detailed within Supplemental Material VI [48].

C. Measurements of a time-modulated metasurface: serrodyne frequency translation

As discussed in Sec. III A, when the metasurface is uniformly biased with a sawtooth reflection phase waveform, serrodyne frequency translation is expected. As shown in Figs. 24 and 25, the reflection amplitude is not unity due to the loss in the metasurface. Therefore, the capacitance-modulation waveform had to be numerically optimized. The optimization process is detailed within Supplemental Material VI [48]. In the experiment, the optimized waveform is sampled of 20 data points per period ($T_p = 40\ \mu$s), and entered into the D/A converter. All channels of the D/A converter are synchronized with the same bias waveform. The bias waveform across several diodes is measured using a differential probe (Tektronix TMDP0200) and Tektronix oscilloscope MDO3024. The optimized and measured bias voltage waveforms are shown in Fig. 26(a) for TE polarization and Fig. 26(c) for TM polarization. The measured reflection spectrum for an oblique angle of 25° is shown in Fig. 26(b) for TE polarization and Fig. 26(d) for TM polarization. Both polarizations show serrodyne frequency translation to $f = f_0 + f_p$. For TE polarization, a 4.604-dB conversion loss and 9.196 dB of sideband suppression are achieved. For TM polarization, a 3.67-dB conversion loss and 9.86-dB sideband suppression are achieved.

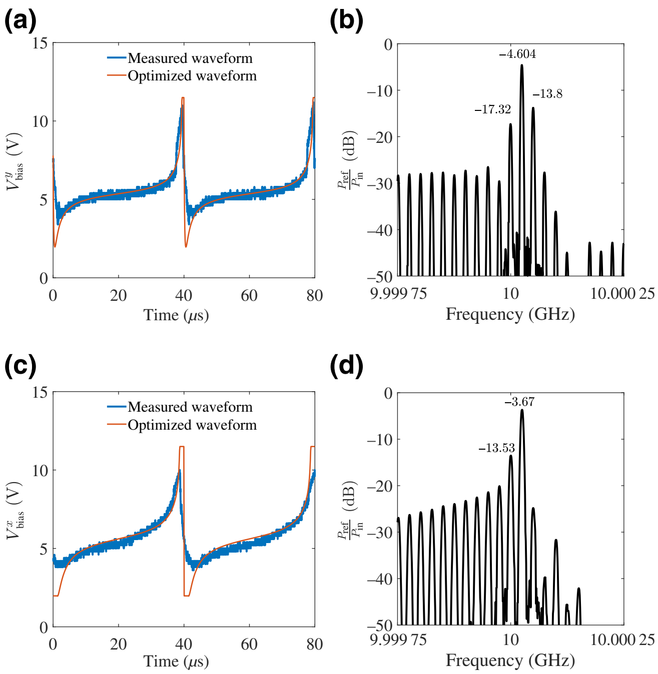

FIG. 26. (a) Bias waveform of the time-modulated metasurface for TE polarization. (b) Measured reflection spectrum of the time-modulated metasurface prototype for TE polarization. (c) Bias waveform of the time-modulated metasurface prototype for TM polarization. (d) Measured reflection spectrum of the time-modulated metasurface for TM polarization.

For each polarization, the measured reflection spectrum in Figs. 26(b) and 26(d) generally agrees with harmonic balance simulations of its extracted circuit models, as shown in Fig. S6 within Supplemental Material VII [48].

V. EXPERIMENTAL VALIDATION OF A SDTWM METASURFACE

In this section, measurements of the prototype metasurface are reported to verify the theory behind SDTWM metasurfaces. Experimental scattering for the three regimes of metasurface operation introduced in Sec. III is reported. Specifically, effects such as specular subharmonic frequency translation, deflective and retroreflective serrodyne frequency translation, and deflective and retroreflective subharmonic frequency translation are experimentally examined. Again, the incident frequency f_0 and modulation frequency f_p are set to 10 GHz and 25 kHz, respectively. Unless stated otherwise, the reflection phase of each column (path) is a sawtooth function in time. The measured conversion loss and sideband suppression for various examples introduced in Sec. III are provided in Table II, and is referred to throughout this section.

A. Small spatial-modulation period ($|k_x \pm \beta_p| > k_0$)

In this section, electrically small spatial-modulation periods are considered ($|k_x \pm \beta_p| > k_0$). The incident wave is chosen to impinge on the metasurface with an oblique angle of 25°. The measured reflection spectra for two-path ($N = 2$) and three-path ($N = 3$) modulation schemes are given in Fig. 27. The reflection spectra are measured at a reflection angle of $\theta = 25°$ (see Fig. 10). The measured spectra for both polarizations clearly demonstrate subharmonic frequency translation, where the only radiated harmonics are those at frequencies $f \; = f \; + rNf_s$ and $r \in \mathbb{Z}$. The measured conversion loss and sideband suppression for both polarizations are reported in examples 1 and 2 in Table II. Compared to the homogenized, lossless metasurface presented in Sec. III B, the conversion loss and sideband suppression degrade more as the number of paths is increased. This is attributed to the evanescent harmonic pairs on the surface of the structure, which is discussed further in Supplemental Material VII [48].

B. Large spatial-modulation period ($|k_x \pm \beta_p| < k_0$)

In this section, the spatial-modulation period is chosen to be electrically large ($|k_x \pm \beta_p| < k_0$). The path number is set to $N = 20$. For the capacitance variation shown in

TABLE II. Measured conversion loss and sideband suppression for desired reflected frequency harmonic f' given: N, the number of paths; θ_i, the incident angle; θ_{obs}, the observation angle, and the temporal phase modulation waveform (either a sawtooth or a sinusoid). Note that positive values of θ_i and θ_{obs} correspond to waves traveling along the positive x direction.

Ex.	N	θ_i	θ_{obs}	Waveform	f'	Conversion loss (dB)		Sideband supression (dB)	
						TE	TM	TE	TM
0	1	25°	25°	saw	$f_0 + f_p$	4.694	3.67	9.196	9.86
1	2	25°	25°	saw	$f_0 + 2f_p$	6.86	5.038	12.71	8.80
2	3	25°	25°	saw	$f_0 + 3f_p$	10.69	8.47	6.55	5.53
3	20	25°	42°	saw	$f_0 + f_p$	5.15	3.74	11.68	15.09
4	20	−42°	−25°	saw	$f_0 + f_p$	5.06	3.79	11.46	15.20
5	4	39°	−39°	saw	$f_0 + 3f_p$	10.85	6.64	9.98	5.45
6	4	−39°	39°	saw	$f_0 + f_p$	4.02	3.39	19.39	15.35
7	4	39°	−39°	sin	$f_0 - f_p$	8.64	5.32	11.97	16.00
8	4	−39°	39°	sin	$f_0 + f_p$	7.76	5.30	9.45	15.87

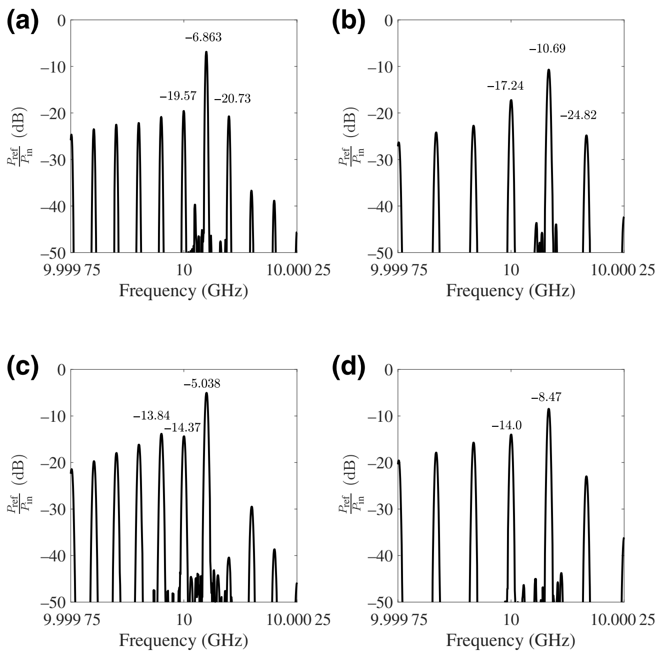

FIG. 27. Measured reflection spectrum of the SDTWM metasurface prototype. (a) Two-path ($N = 2$) modulation for TE polarization. (b) Three-path ($N = 3$) modulation for TE polarization. (c) Two-path ($N = 2$) modulation for TM polarization. (d) Three-path ($N = 3$) modulation for TM polarization.

Figs. 26(a) and 26(c), the metasurface acts as a serrodyne frequency translator, that simultaneously deflects the wave to a different angle. When the incident angle is $\theta_1 = 25^\circ$, the measured reflection spectra at the reflection angle $\theta_2 = 42^\circ$ is shown in Fig. 28. The spectra for both polarizations clearly show a Doppler shift to frequency $f_0 + f_p$. The measured conversion loss and sideband suppression for both polarizations are provided in example 3 in Table II. Note that the reflection angles for harmonics with frequency f_0 and $f_0 + 2f_p$ are 25° and 67°, respectively. We can see from Fig. 28 that a fraction of the reflected power from these two harmonics is still captured by the finite aperture of the receive antenna due to its relatively close proximity to the metasurface.

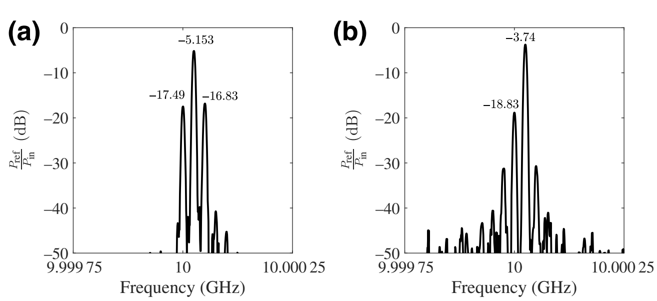

FIG. 28. Measured reflection spectrum of the SDTWM metasurface prototype with an incident angle of 25°. (a) 20-path ($N = 20$) modulation for TE polarization. (b) 20-path ($N = 20$) modulation for TM polarization.

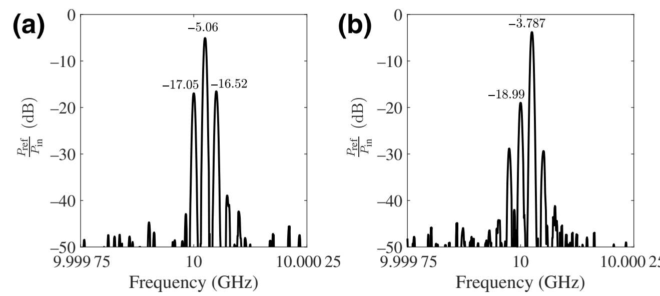

FIG. 29. Measured reflection spectrum of the SDTWM metasurface prototype with an incident angle of −42°. (a) 20-path ($N = 20$) modulation for TE polarization. (b) 20-path ($N = 20$) modulation for TM polarization.

By simply interchanging the transmitting and receiving antennas, we can measure the reflection spectra for the case where the incident angle is $\theta_2 = -42^\circ$. The measured reflected spectra at the reflection angle of $\theta_1 = -25^\circ$ are given in Fig. 29. Again, the spectra for both polarizations clearly show a Doppler shift to a frequency $f_0 + f_p$. The measured conversion loss and sideband suppression for both polarizations are reported in example 4 in Table II. The harmonics with frequency f_0 and $f_0 + 2f_p$ are reflected at −42° and 9.74°, respectively, which are also captured by the receiving antenna. Note that, the reflected spectra in Figs. 28 and 29 are almost identical. This is due to the fact that the modulation frequency is far lower than the signal frequency. Otherwise, the reflection angle would differ from $\theta_1 = -25^\circ$, as discussed within Supplemental Material V.

C. Wavelength-scale spatial-modulation period ($|k_x| + |\beta_p| > k_0$ and $||k_x| - |\beta_p|| < k_0$)

In this section, the spatial-modulation period is on the order of the wavelength of radiation ($|k_x| + |\beta_p| > k_0$ and $||k_x| - |\beta_p|| < k_0$). The path number is chosen to be $N = 4$. As in Sec. III D, the retroreflective angle is chosen to be ±39°. In experiment, a 3-dB directional coupler (Omni-spectra 2030-6377-00) is attached to the antenna in order to measure the retroreflected spectra. Note that the modulation waveform on each column is optimized with the same procedure given within Supplemental Material VI [48], for an incident angle of 39°. In this section, the retroreflective behavior of the metasurface is experimentally verified for the various scenarios introduced in Sec. III D.

1. Measured retroreflective subharmonic frequency translation

The measured retroreflection spectra at an oblique angle of 39° are given in Figs. 30(a) and 30(c) for TE and TM

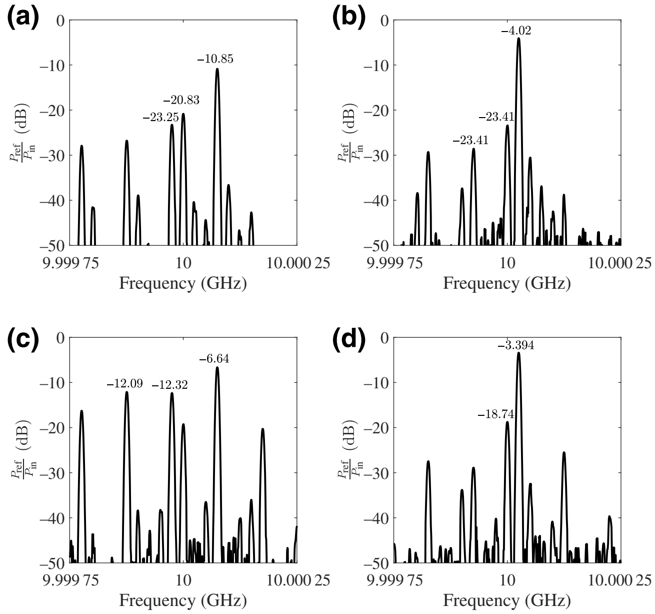

FIG. 30. Measured retroreflection spectrum of the SDTWM metasurface prototype. (a) 4-path ($N = 4$) modulation for TE polarization for an incident angle of 39°. (b) 4-path ($N = 4$) modulation for TE polarization for an incident angle of −39°. (c) 4-path ($N = 4$) modulation for TM polarization for an incident angle of 39°. (d) 4-path ($N = 4$) modulation for TM polarization for an incident angle of −39°.

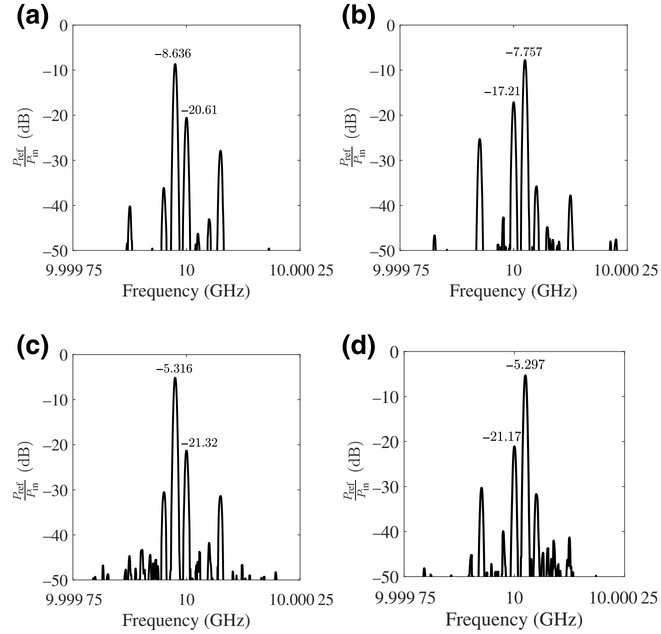

FIG. 31. Measured retroreflection spectrum of the SDTWM metasurface prototype. The bias waveform generates a sinusoidal reflection phase. (a) Four-path ($N = 4$) modulation for TE polarization for an incident angle of 39°. (b) Four-path ($N = 4$) modulation for TE polarization for an incident angle of −39°. (c) Four-path ($N = 4$) modulation for TM polarization for an incident angle of 39°. (d) Four-path ($N = 4$) modulation for TM polarization for an incident angle of −39°.

polarization, respectively. As predicted, frequency translation to $f_0 + 3f_p$ is observed for both polarizations. The measured conversion loss and sideband suppression for both polarizations are reported in example 5 in Table II. Note that, comparing Figs. 30(a) and 30(c) to Figs. 18(a) and 18(c), only the harmonics in solid lines are captured by the antenna.

For an incident angle of −39°, the measured retroreflection spectra are shown in Figs. 30(b) and 30(d) for TE and TM polarization, respectively. As predicted, the spectra for both polarizations show a Doppler shift to frequency $f_0 + f_p$. The measured conversion loss and sideband suppression for both polarizations are reported in example 6 in Table II. Again, comparing Figs. 30(b) and 30(d) to Figs. 18(b) and 18(d), only the harmonics in solid lines are captured by the antenna.

2. Measured retroreflective frequency translation with a staggered sinusoidal reflection phase

In this section, the bias waveforms on adjacent columns generate staggered sinusoidal reflection phases. The measured retroreflection spectra at an oblique angle of 39° are given in Figs. 31(a) and 31(c). As predicted, frequency translation to $f_0 - f_p$ is observed for both polarizations. The measured conversion loss and sideband suppression for both polarizations are provided in example 7 of Table II. The measured retroreflection spectra at an oblique angle of −39° are given in Figs. 31(b) and 31(d). Frequency translation to $f_0 + f_p$ is observed for both polarizations. The measured conversion loss and sideband suppression for both polarizations are provided in example 8 of Table II.

Note that, both of the two retroreflection cases used four paths per spatial-modulation period for a retroreflection angle of 39° (examples 5 and 7 of Table II). The only difference between the two cases was the time dependence of the reflection phase (sawtooth versus sinusoidal). Thus, we show that simply changing the temporal-modulation waveform of the stixels, the retroreflection frequency can be changed. In this case, it changes from $f_0 - f_p$ to $f_0 + 3f_p$.

VI. CONCLUSION

This work theoretically and experimentally studies spatially discrete, travelling-wave modulated (SDTWM) metasurfaces. A modified Floquet analysis of the SDTWM metasurface is presented based on a new boundary condition that is established within SDTWM structures. The analysis allows the separation of the macroscopic and microscopic spatial variations of the field on the metasurface. The macroscopic spatial variation is enforced by the modulation wavelength, while the microscopic spatial variation accounts for the field variation across each constituent stixel. The analysis presented in this paper provides an accurate model of the metasurface and serves as a guide for designing practical space-time metasurfaces. Most importantly, the analysis provides physical insight into SDTWM metasurfaces and reveals various phenomena including subharmonic frequency translation in specular or deflected directions. Such a phenomenon is not possible with the continuous traveling-wave modulation commonly assumed in previous studies.

In this paper, the operation of a SDTWM metasurface is categorized into three regimes. When the spatial-modulation period is electrically large, the metasurface allows simultaneous frequency translation and angular deflection. Tuning the spatial-modulation period allows the metasurface to steer the reflected beam, and even exhibit retroreflection. When the spatial-modulation period is electrically small, the metasurface exhibits subharmonic frequency translation. In this case, all the radiated harmonics are reflected in the specular direction for low frequencies of modulation. When the spatial-modulation period is on the order of a wavelength, subharmonic frequency translation and deflection can be achieved. It is also shown that the frequency of the deflected wave can be changed by modifying the temporal-modulation waveform.

To verify the analysis, a proof-of-principle metasurface is designed and fabricated at X-band frequencies. Measurements show good agreement with theoretical predictions in the three operating regimes of the metasurface. The designed metasurface provides a new level of reconfigurability. Multiple functions including beam steering, retroreflection, serrodyne frequency translation, and subharmonic frequency translation are achieved with the ultrathin (0.06λ) metasurface by appropriately tailoring the SDTWM waveform. The designed metasurface could find various applications in next-generation communication, imaging, and radar systems.

ACKNOWLEDGMENTS

This work is supported by the AFOSR MURI program FA9550-18-1-0379 and by DSO National Laboratories under Contract No. DSOCO15027.

[1] M. Manjappa, P. Pitchappa, N. Singh, N. Wang, N. I. Zheludev, C. Lee, and R. Singh, Reconfigurable MEMS fano metasurfaces with multiple-input–output states for logic operations at terahertz frequencies, Nat. Commun. **9**, 1 (2018).

[2] T. Roy, S. Zhang, I. W. Jung, M. Troccoli, F. Capasso, and D. Lopez, Dynamic metasurface lens based on MEMS technology, APL Photonics **3**, 021302 (2018).

[3] L. Cong, P. Pitchappa, C. Lee, and R. Singh, Active phase transition via loss engineering in a terahertz MEMS metamaterial, Adv. Mater. **29**, 1700733 (2017).

[4] Z. Wu, Y. Ra’di, and A. Grbic, Tunable Metasurfaces: A Polarization Rotator Design, Phys. Rev. X **9**, 011036 (2019).

[5] J. Lončar, A. Grbic, and S. Hrabar, A reflective polarization converting metasurface at x-band frequencies, IEEE Trans. Antennas Propag. **66**, 3213 (2018).

[6] Q. Wang, E. T. Rogers, B. Gholipour, C.-M. Wang, G. Yuan, J. Teng, and N. I. Zheludev, Optically reconfigurable metasurfaces and photonic devices based on phase change materials, Nat. Photonics **10**, 60 (2016).

[7] T. G. Folland, A. Fali, S. T. White, J. R. Matson, S. Liu, N. A. Aghamiri, J. H. Edgar, R. F. Haglund, Y. Abate, and J. D. Caldwell, Reconfigurable infrared hyperbolic metasurfaces using phase change materials, Nat. Commun. **9**, 1 (2018).

[8] Y. Fan, N.-H. Shen, T. Koschny, and C. M. Soukoulis, Tunable terahertz meta-surface with graphene cut-wires, ACS Photonics **2**, 151 (2015).

[9] Y. Yao, R. Shankar, M. A. Kats, Y. Song, J. Kong, M. Loncar, and F. Capasso, Electrically tunable metasurface perfect absorbers for ultrathin mid-infrared optical modulators, Nano Lett. **14**, 6526 (2014).

[10] N. M. Estakhri and A. Alù, Recent progress in gradient metasurfaces, JOSA B **33**, A21 (2016).

[11] A. V. Kildishev, A. Boltasseva, and V. M. Shalaev, Planar photonics with metasurfaces, Science **339**, 1232009 (2013).

[12] C. Pfeiffer and A. Grbic, Bianisotropic Metasurfaces for Optimal Polarization Control: Analysis and Synthesis, Phys. Rev. Appl. **2**, 044011 (2014).

[13] N. Yu and F. Capasso, Flat optics with designer metasurfaces, Nat. Mater. **13**, 139 (2014).

[14] M. Liu, D. A. Powell, Y. Zarate, and I. V. Shadrivov, Huygens’ Metadevices for Parametric Waves, Phys. Rev. X **8**, 031077 (2018).

[15] Z. Wu and A. Grbic, Serrodyne frequency translation using time-modulated metasurfaces, IEEE Trans. Antennas Propag. **68**, 1599 (2020).

[16] Z. Wu and A. Grbic, in *2019 IEEE International Symposium on Antennas and Propagation and USNC-URSI Radio Science Meeting* (IEEE, Montréal, Québec, Canada, 2019), p. 1609.

[17] A. Shaltout, A. Kildishev, and V. Shalaev, Time-varying metasurfaces and Lorentz non-reciprocity, Opt. Mater. Express **5**, 2459 (2015).

[18] A. M. Shaltout, V. M. Shalaev, and M. L. Brongersma, Spatiotemporal light control with active metasurfaces, Science **364**, eaat3100 (2019).

[19] Y. Hadad, D. Sounas, and A. Alu, Space-time gradient metasurfaces, Phys. Rev. B **92**, 100304 (2015).

[20] C. Caloz and Z.-L. Deck-Léger, Spacetime metamaterials, part I: General concepts, IEEE Trans. Antennas Propag. **68**, 1569 (2019).

[21] M. M. Salary, S. Jafar-Zanjani, and H. Mosallaei, Electrically tunable harmonics in time-modulated metasurfaces for wavefront engineering, New J. Phys. **20**, 123023 (2018).

[22] J. Zang, D. Correas-Serrano, J. Do, X. Liu, A. Alvarez-Melcon, and J. Gomez-Diaz, Nonreciprocal Wavefront

Engineering with Time-Modulated Gradient Metasurfaces, Phys. Rev. Appl. **11**, 054054 (2019).

[23] S. Taravati and G. V. Eleftheriades, Generalized Space-Time-Periodic Diffraction Gratings: Theory and Applications, Phys. Rev. Appl. **12**, 024026 (2019).

[24] Y. Shi and S. Fan, Dynamic non-reciprocal meta-surfaces with arbitrary phase reconfigurability based on photonic transition in meta-atoms, Appl. Phys. Lett. **108**, 021110 (2016).

[25] X. Wang, A. Díaz-Rubio, H. Li, S. A. Tretyakov, and A. Alù, Theory and Design of Multifunctional Space-Time Metasurfaces, Phys. Rev. Appl. **13**, 044040 (2020).

[26] S. Taravati and A. A. Kishk, Advanced wave engineering via obliquely illuminated space-time-modulated slab, IEEE Trans. Antennas Propag. **67**, 270 (2018).

[27] S. Taravati, N. Chamanara, and C. Caloz, Nonreciprocal electromagnetic scattering from a periodically space-time modulated slab and application to a quasisonic isolator, Phys. Rev. B **96**, 165144 (2017).

[28] N. A. Estep, D. L. Sounas, J. Soric, and A. Alù, Magnetic-free non-reciprocity and isolation based on parametrically modulated coupled-resonator loops, Nat. Phys. **10**, 923 (2014).

[29] D. L. Sounas, C. Caloz, and A. Alu, Giant non-reciprocity at the subwavelength scale using angular momentum-biased metamaterials, Nat. Commun. **4**, 2407 (2013).

[30] C. Doerr, L. Chen, and D. Vermeulen, Silicon photonics broadband modulation-based isolator, Opt. Express **22**, 4493 (2014).

[31] S. Taravati and G. V. Eleftheriades, Full-Duplex Nonreciprocal Beam Steering by Time-Modulated Phase-Gradient Metasurfaces, Phys. Rev. Appl. **14**, 014027 (2020).

[32] S. Young (personal communication).

[33] C. Scarborough and A. Grbic, Accelerated n-path network analysis using the floquet scattering matrix method, IEEE Trans. Microw. Theory Tech. **68**, 1248 (2020).

[34] J. A. Richards, *Analysis of Periodically Time-Varying Systems* (Springer Science & Business Media, New York, USA, 2012).

[35] N. Reiskarimian and H. Krishnaswamy, Magnetic-free non-reciprocity based on staggered commutation, Nat. Commun. **7**, 11217 (2016).

[36] A. Ghaffari, E. A. Klumperink, M. C. Soer, and B. Nauta, Tunable high-q n-path band-pass filters: Modeling and verification, IEEE J. Solid-State Circuits **46**, 998 (2011).

[37] R. Shrestha, E. Mensink, E. A. Klumperink, G. J. Wienk, and B. Nauta, in *2006 IEEE International Solid State Circuits Conference-Digest of Technical Papers* (IEEE, San Francisco, CA, USA, 2006), p. 1800.

[38] L. Franks and I. Sandberg, An alternative approach to the realization of network transfer functions: The n-path filter, Bell Syst. Tech. J. **39**, 1321 (1960).

[39] D. Von Grunigen, R. Sigg, J. Schmid, G. Moschytz, and H. Melchior, An integrated CMOS switched-capacitor bandpass filter based on n-path and frequency-sampling principles, IEEE J. Solid-State Circuits **18**, 753 (1983).

[40] A. Ghaffari, E. A. Klumperink, and B. Nauta, in *2010 IEEE Radio Frequency Integrated Circuits Symposium* (IEEE, Anaheim, California, USA, 2010), p. 299.

[41] R. Weiss and E. Cohen, in *2017 IEEE International Conference on Microwaves, Antennas, Communications and Electronic Systems (COMCAS)* (IEEE, Tel, Aviv, Israel, 2017), p. 1.

[42] J. Zhou, N. Reiskarimian, and H. Krishnaswamy, in *63rd IEEE International Solid-State Circuits Conference, ISSCC 2016* (Institute of Electrical and Electronics Engineers Inc., San Francisco, CA, USA, 2016), p. 178.

[43] C. Scarborough and A. Grbic, in *2020 14th International Congress on Artificial Materials for Novel Wave Phenomena (Metamaterials)* (2020).

[44] C. Scarborough and A. Grbic, in *2019 IEEE International Symposium on Antennas and Propagation and USNC-URSI Radio Science Meeting* (IEEE, Atlanta, GA, 2019), p. 199.

[45] D. F. Sievenpiper, J. H. Schaffner, H. J. Song, R. Y. Loo, and G. Tangonan, Two-dimensional beam steering using an electrically tunable impedance surface, IEEE Trans. Antennas Propag. **51**, 2713 (2003).

[46] D. Ramaccia, D. L. Sounas, A. Alù, A. Toscano, and F. Bilotti, Phase-induced frequency conversion and doppler effect with time-modulated metasurfaces, IEEE Trans. Antennas Propag. **68**, 1607 (2020).

[47] O. Luukkonen, M. G. Silveirinha, A. B. Yakovlev, C. R. Simovski, I. S. Nefedov, and S. A. Tretyakov, Effects of spatial dispersion on reflection from mushroom-type artificial impedance surfaces, IEEE Trans. Microw. Theory Tech. **57**, 2692 (2009).

[48] See Supplemental Material http://link.aps.org/supplemental/10.1103/PhysRevApplied.14.064060, which includes Refs. [50,51].

[49] M. T. Solutions, Solderable GaAs Constant Gamma Flip-Chip Varactor Diode, MAVR-000120-1411, available at https://www.macom.com/products/product-detail/MAVR-000120-14110P.

[50] L. Tsang, J. A. Kong, and K.-H. Ding, *Scattering of Electromagnetic Waves: Theories and Applications* (John Wiley & Sons, Hoboken, New Jersey, 2004), Vol. 27.

[51] R. E. Collin, *Foundations for Microwave Engineering* (John Wiley & Sons, Hoboken, New Jersey, 2007).